Precipitation-site competition in duplex stainless steels: Cu clusters vs spinodal decomposition interfaces as nucleation sites during thermal aging

Timothy G. Lach[1]*, William E. Frazier[2], Jing Wang[2], Arun Devaraj[3], and Thak Sang Byun[1]

[1]Materials Science and Technology Division, Oak Ridge National Laboratory, 1 Bethel Valley Road, Oak Ridge, TN 37830
[2]Energy and Environment Directorate, Pacific Northwest National Laboratory, 902 Battelle Boulevard. Richland, WA 99352
[3]Physical and Computational Sciences Directorate, Pacific Northwest National Laboratory, 902 Battelle Boulevard. Richland, WA 99352 USA

*corresponding author: lachtg@ornl.gov

Keywords: Duplex stainless steel; Thermal aging; Precipitation; Atom probe tomography (APT); Kinetic Monte Carlo

Declarations of interest: none

ABSTRACT

Competing microstructural evolution mechanisms can exist simultaneously when duplex stainless steels are operating for several decades in a high temperature service environment. Such competition between different microstructural evolution pathways can be difficult to ascertain using simple model alloy systems necessitating detailed microstructural analysis of phase transformation mechanisms in complex alloys. Thus, duplex stainless steels with complex but well understood chemistries were used to investigate the relative importance of different heterogeneous nucleation sites – specifically, spinodal decomposition and Cu clustering – on Ni-Si-Mn precipitation during thermal aging. Precipitation of Ni-Si-Mn particles in ferrite-bearing steels during thermal aging and irradiation can greatly change mechanical properties. Using duplex stainless steels with custom-modified compositions along with advanced microstructural characterization and first-passage kinetic Monte Carlo simulations, it is revealed that while the interface between Cr and Fe formed during spinodal decomposition can be a pathway for solute diffusion, it is not a preferred site for Ni-Si-Mn precipitation. Instead, the presence of a higher concentration of Cu leads to the formation of small Cu-rich clusters with high energy interfaces that act as nucleation sites for Ni-Si-Mn particles. These results will inform predictive models for the use of precipitation-hardened alloys for extended operation at high temperatures.

1. INTRODUCTION

In complex, multicomponent structural alloys designed for operating at elevated temperatures for extended periods of time up to several decades, there can be multiple phase transformation mechanisms that can happen concurrently and potentially interdependently. Often, the understanding of microstructural evolution pathways of simpler model alloys is used to predict the behavior of more complex multicomponent alloys during such extended use in service[1–3]. However, the interdependencies among different microstructural evolution pathways may not be observed in model alloys. The competition between these disparate but potentially concurrent mechanisms of microstructural evolution needs to be understood at a near atomic scale resolution to develop an efficient predictive model for microstructural evolution of these alloys. For example, steel components with complex compositions in nuclear light water reactor (LWR) systems are subjected to high temperature (270-350 ˚C) and/or radiation conditions. In order to improve LWR sustainability and extend LWR lifetimes up to 80 years or more, predictive models are essential for the microstructural and property evolution of these alloys over extended operation in these conditions[4,5]. Multi-component alloys used in nuclear reactors like duplex stainless steels, ferritic steels, reactor pressure vessel (RPV) steels, and high entropy alloys can have microstructures that evolve through different mechanisms such as precipitation, co-precipitation, and spinodal decomposition, resulting in deleterious properties[6–9].

In the ferrite phase of duplex stainless, ferritic, and RPV steels, thermal aging or ion/ neutron radiation causes the nucleation and growth of Ni, Si, and Mn-rich precipitates, or the so-called "late blooming phase"[10–14]. The nucleation and growth of these particles lead to a corresponding growth in hardness of the ferrite phase, potentially causing embrittlement; thus, it is important to understand what factors influence the precipitation of Ni-Si-Mn-rich particles. In the low Cr RPV steels, mostly with tempered bainitic or martensitic structure, precipitation of Ni-Si-Mn-rich particles during thermal aging at ~330-400 ˚C occurs as core-shell or appendage-shaped particles with Cu-rich cores and Ni-Si-Mn-rich shells[15–18]. This occurs because Cu is highly immiscible in Fe and Cr, but the interfacial energy of (Fe, Cr)-Cu is high; therefore, Ni (and Si and Mn) reduce the interfacial energy of these Cu clusters[11]. This same phenomenon is found in high Cr irradiated steels as well[18].

In high Cr ferritic steels or duplex stainless steels like cast austenitic stainless steels (CASS), it has been widely presented that Ni-Si-Mn-rich particles precipitate primarily at the α/α' interfaces formed by spinodal decomposition during thermal aging at moderate temperatures and the combination of which lead to mechanical property degradation[19–27]. Spinodal decomposition is the spontaneous separation of a phase into two separate phases due to a miscibility gap in the phase diagram[28]. The kinetics of spinodal decomposition can be enhanced by temperature or composition, with increased temperature enhancing diffusion and additions of certain alloying elements increasing the driving force for decomposition. During thermal aging below 475 ˚C in high-Cr Fe-Cr alloys such as duplex stainless steels, the δ-ferrite decomposes into Fe-rich α-phase and Cr-rich α'-phase due to the miscibility gap up to that temperature. This decomposition is enhanced with additional Cr and with additions of alloying elements of Ni[29–31] and Mo[32], as these increase the immiscibility within the ferrite phase. Multiple researchers have determined that precipitation of Ni-Si-Mn particles occurs at the interface between α and α' because these elements are rejected from these phases during spinodal decomposition where they precipitate when a

necessary concentration is reached[6,19,33,34]. In our previous work, Ni-Si-Mn-rich G-phase ($Ni_{16}Si_7Mn_6$) precipitates were observed at the α/α' interfaces, but also had Cu-rich co-precipitates attached[35,36]. These CASS alloys had elevated amounts of Cu in the ferrite phase (>0.2at%). However, no studies have been done to determine the effects of elevated Cu on Ni-Si-Mn precipitation in cast austenitic stainless steels or other high Cr (>20at%), high Ni (>5at%) alloys. This work allows for the direct comparison with the low Cr but elevated Cu steels to determine the interdependencies of these different mechanisms found in complex multicomponent alloys.

In this study, thermal aging up to 10,000 hours at 290-400 ˚C of two sets of two common CASS alloys (CF8 and CF3) has been completed; these alloys are the cast equivalents of 304 and 304L wrought stainless steels, respectively. Thermal aging without radiation was performed because thermal aging is the dominant phenomena in these alloys in LWR coolant systems[37,38]. High Cu and low Cu/ higher Cr/ Ni versions of each alloy were used to elucidate whether α/α' interfaces or Cu clusters produce more Ni-Si-Mn precipitation. The higher Cr alloys would have a larger amplitude and wavelength of spinodal decomposition with aging but limited Cu clustering, while the high Cu alloys would have more Cu clustering but less spinodal decomposition. Thus, the relative importance of each can be determined. This study quantitatively evaluates thermal aging-induced microstructural changes in the ferrite phase of the CASS alloys using atom probe tomography (APT), which can resolve and quantify the degree of spinodal decomposition and precipitation with high spatial and elemental resolution[39–41]. The APT results were compared to first-passage kinetic Monte Carlo (FPKMC) simulations to elucidate mechanisms for precipitation in these alloys[42]. The results presented here will increase the understanding of precipitation in multi-phase alloy systems, and it will help determine which alloy designs and compositions are least susceptible to thermal aging degradation.

2. MATERIALS AND METHODS

2.1 Materials and Thermal Aging

Four sets of CASS alloys are being evaluated for thermal aging degradation mechanisms and the effect of alloy composition on these mechanisms. In this study, two sets of alloys, designated as alloys A (CF3) and C (CF8) in Table 1, were cast into ~15 kg cylindrical ingots (~8 cm diameter × ~35 cm long). No further heat treatment was applied. The other two alloys, designated as alloys B (CF3) and D (CF8) in Table 1, were cast statically (alloy B) and centrifugally (alloy D) as part of much larger castings. The compositions in atomic percent (or atomic ppm for carbon) are presented in Table 1 as determined by Dirats Laboratories using inductively coupled plasma – mass spectrometry (ICP-MS). While the alloy grades – CF3 and CF8 – are designated for a maximum of 300 or 800 weight ppm respectively, we have adjusted the composition to reflect atomic percent and ppm to stay consistent with analysis throughout this study. The compositions of all four alloys are within the ASTM specifications for these grades. These compositions are of the alloy, including both the matrix austenite phase and the ferrite phase. The compositions of each phase will be weighted more heavily with elements that are austenite-stabilizers or ferrite-stabilizers, respectively. Table 2 takes this into account and presents the average composition of the ferrite phase as measured by APT reconstructions. The concentrations of Ni, Si, Mn, and Cu are highlighted as they are the primary differences among the alloys that are known to be incorporated into G-phase precipitates. Those elements along with Cr have a consistent difference

between the two sets of alloys – A and C have less Cr and Ni, and more Mn and Cu than alloys B and D. While alloys A and C will be denoted as "high Cu" in much of this article, the amount of Cu is still relatively low compared to other similar steels[15,16].

Table 1: Bulk alloy at% of four cast alloys (noted with their wrought equivalents) – C atom ppm

Sample Alloy	Grade	Fe	Cr	Ni	Si	Mn	Cu	C (ppm)	Mo	P
A	**CF3 (304L)**	Bal	20.22	7.58	1.93	1.44	0.35	1196	0.19	0.05
B	**CF3 (304L)**	Bal	21.76	8.92	2.14	0.89	0.09	1002	0.08	0.04
C	**CF8 (304)**	Bal	19.70	8.31	2.47	1.10	0.25	3029	0.17	0.05
D	**CF8 (304)**	Bal	21.02	8.01	2.55	0.57	0.06	2683	0.17	0.05

Table 2: Ferrite composition (at%) of four cast alloys as measured by APT

Sample Alloy	Grade	Fe	Cr	Ni	Si	Mn	Cu	C	Mo	P
A	**CF3 (304L)**	62.79 ±0.64	26.68 ±0.80	5.44 ±0.25	3.25 ±0.04	1.03 ±0.20	0.22 ±0.04	0.02 ±0.01	0.17 ±0.04	0.14 ±0.03
B	**CF3 (304L)**	59.84 ±0.36	29.83 ±0.46	6.35 ±0.17	2.65 ±0.20	0.85 ±0.10	0.06 ±0.01	0.05 ±0.07	0.16 ±0.02	0.08 ±0.06
C	**CF8 (304)**	62.54 ±0.69	26.81 ±0.24	5.49 ±0.15	3.27 ±0.07	1.05 ±0.26	0.22 ±0.04	0.02 ±0.01	0.19 ±0.07	0.15 ±0.05
D	**CF8 (304)**	60.11 ±0.47	29.05 ±0.42	6.18 ±0.02	3.38 ±0.02	0.59 ±0.02	0.06 ±0.00	0.03 ±0.04	0.33 ±0.01	0.16 ±0.01

The alloys have been aged at four different temperatures in four large muffle furnaces (MTI Co. Model KSL-1200X-L). The chamber temperatures are controlled by UDIAN programmable controllers at an accuracy of <±1 ˚C using K-type thermocouples; the spatial temperature variation within chamber is ±5 ˚C. Aging temperatures were set at 290, 330, 360, and 400 ˚C. At this point in the long-term study, sets of material have been retrieved from the furnaces after 1,500 and 10,000 hours of aging. These aging treatments were chosen to produce a range of conditions giving the under-aged (for the lower aging temperatures) and over-aged conditions (for the highest aging temperature and time) for the alloys when compared to LWR service conditions for 60 to 80 years[5].

2.2 Microstructural and Elemental Characterization

Scanning transmission electron microscopy (STEM) and APT were used to characterize the microstructural evolution and elemental distribution of the alloys. STEM was conducted on an aberration-corrected JEOL ARM200F TEM/ STEM with bright field (BF) and high angle annular dark field (HAADF) micrographs obtained in STEM mode. As will be shown in the results, quantitative and qualitative information were difficult to achieve with the large number density of particles in these samples and for determining the interplay among the Ni-Si-Mn particles, spinodal

decomposition, and Cu clustering. Thus, APT was used to do this; it was performed on a Cameca LEAP 4000XHR using voltage mode with a pulse fraction of 20% and detection rate of 0.005 atoms/pulse, pulse repetition rate of 200 kHz while maintaining needle specimen temperature at 45 K.

STEM and APT specimens were thinned/ sharpened using the focused ion beam/ scanning electron microscope (FIB/SEM) (FEI Helios NanoLab 660 or FEI Quanta) annular milling technique with lift-outs centered in the ferrite phase and placed on 6×6 Si micro-tip arrays[43]. Ga-ion damage was minimized using low voltage (2 keV) and low current final sharpening. Reconstructions and analyses for APT were performed using Cameca's Integrated Visualization and Analysis Software 3.8.2 (IVAS) using standard techniques that include radial distribution functions (RDF) and isoconcentration surface-based cluster analysis[43–45]. Similar mass/ charge range files with only minor adjustments between reconstructions were used to reduce potential artefacts in compositional analyses among the various samples. The tip profile reconstruction method was used for determining the initial radius of the reconstruction using high resolution SEM images of the final tip. A fixed image compression factor of 1.66 was used as no clear pole locations were found within the field ion micrographs. Global background subtraction was used for determining composition. Peak overlaps were considered but determined to have a minimal effect for the purposes of this study. Only 0.3% of natural abundance Fe (^{58}Fe) has an overlap with the majority Ni isotope, ^{58}Ni. ^{54}Fe does have an overlap with ^{54}Cr, but the comparison of natural relative abundances relative to peak height matched it with Fe more so than Cr. Also, the relative abundance of these two isotopes is small. ^{28}Si with a 1+ charge state does overlap significantly ^{56}Fe in the 2+ charge state; however, only the Si 2+ charged states were used for Si as the natural abundances for each set of 2+ charge state peaks, for Si and Fe respectively, matched well. Another overlap is the peak at 32 Da, where the ^{64}Ni 2+ peak overlaps with the ^{96}Mo 3+ peak. Relative to the natural abundances of the other isotopes, this peak was found to be mostly Ni. Also, the majority of Mo is found in the 2+ charge state.

Cluster analysis was done based on equivalent aging time, t, at a LWR relevant temperature of 320 ˚C using the following equation:

$$t = t_0\left(\frac{Q}{R}\left(\frac{1}{593} - \frac{1}{T}\right)\right) \qquad (1)$$

Where t_o is the actual aging time at temperature, T; Q is the activation energy; and R is the gas constant. Prior research has described the activation energy for both spinodal decomposition and G-phase precipitation as being approximately the same at 243 ±80 kJ/mol for temperatures between 320 ˚C and 400 ˚C[25,37,46,47]. In this study, we will use the bottom end of that range using 160 kJ/mol. While it is on the low end of previous research, it is a usable value for the basis of this study as it best fits the data. All the data will also be plotted in the supplemental material using 243 kJ/mol for comparison. Future work that includes longer term aging will investigate the actual activation energy value for G-phase precipitation compared to spinodal decomposition.

RDF analyses of individual elements in APT data can offer great insights not only to the degree with which the elements segregate but also to which other elements they most strongly interact[45]. RDF analysis provides an average radial concentration around each atom in the APT reconstruction data for a particular element as a function of radial distance from the center atom.

This average radial concentration profile for each element, when divided by the average bulk concentration of that element, provides the bulk normalized concentration plots. A value of 1 for bulk normalized concentration corresponds to a random distribution or no correlation with the designated element. A value above 1 indicates attraction with the "center atom" element. A value less than 1 indicates a repulsive interaction with the designated element. "X-Cr" RDF plots are used for analyzing spinodal decomposition, where "X" signifies a given element relative to the Cr "center atom".

For spinodal decomposition, the Cr-Cr (Cr concentration relative to Cr atoms) RDF plots for each alloy at each aging temperature and time enables us to quantify the extent of spinodal decomposition in the different alloys by determining the compositional amplitude and spatial wavelength of decomposition[45,48]. The Cr concentration is assumed to be a sinusoidal wave function with a wavelength λ, and position vector defined along with the compositional amplitude fluctuation A calculated using the bulk normalized concentration in the Cr-Cr RDF value at a distance of 0 nm (RDF(0nm)) using the following equations:

$$f(\vec{r}) = C_0 + \frac{A}{2}\sin\left(\left(\frac{2\pi}{\lambda}\right)(\vec{r})\right) \qquad (2)$$

$$A = C_0\sqrt{2(RDF(0nm) - 1)} \qquad (3)$$

where C_0 is the bulk Cr composition of the atom probe reconstruction[49]. The spatial wavelength is captured by the distance of a second peak in the Cr-Cr RDF plot. This second peak specifies a statistically nearest distance between two Cr-rich regions in three-dimensions, and thus in this case, indicates the wavelength of the spinodal decomposition[45,48]. RDF analyses were also carried out on all the major elements – Fe, Cr, Ni, Si, Mn, and Cu. While a wavelength between particles cannot be ascertained, the degree of interaction between elements can be quantified using the 0nm value (or "amplitude") and thus help determine the mechanisms for clustering. Error in RDF values were determined using point counting statistical propagation of error. As will be shown, these error values are small.

Cluster analysis in APT data is a classic unsupervised machine learning problem, and like many other problems in this category, it lacks a clear metric/loss function to define a quality of prediction or a confidence level of the result. In this study, we employed the isoconcentration surface (or isosurface) method for Ni-Si-Mn and Cu clusters identification[50]. It is a simple yet widely used technique to identify clusters by constructing a constant concentration surface based on local solute concentration, and the enclosed ions are identified as a cluster. This technique has great flexibilities and need only one user input as concentration threshold. Like many other methods for unsupervised machine learning problems, parameter selection can be subjective. In many cluster analyses for APT, the de facto rule of thumb is that identified clusters should be matching human visualized inspection as much as possible. The concentration threshold is kept constant for all datasets since we are interested in the cluster size evolution, which is directly affected by the threshold choice. However, the selection of parameters may lead to some uncertainties for cluster identification in low aging temperature or low effective aging time datasets. This is due to some clusters having much lower solute concentration in these conditions. However, we believe the

corresponding volume fraction trend is preserved despite the minor uncertainties. A direct comparison between two concentration thresholds are shown in supplementary Figure S6.

In addition, we can see that the uncertainties are small by comparing values with STEM micrographs and comparison with the OPTICS-APT method for cluster analysis[51] as discussed in section 3. The OPTICS-APT method is based on reachability distance, which is an inverse analogue to local atomic density. It is designed to overcome issues with using a global density threshold and is capable to detect clusters of varying densities using one set of parameters. The maximum search distance ε is set to 2 nm, which is large enough to ensure all atoms are considered potential cluster atoms. The lower bound for cluster solute atoms, MinPts, is set to 50, which is typical value for cluster of this size and solute concentration. A post-processing parameter, the background reachability distance, r_{bg}, is set to 2-2.5 nm, depending on datasets. The value can be easily determined by the user through investigating the corresponding reachability distance histogram, which is likely a bimodal distribution, to separate data and background. While the OPTICS-APT method can properly identify clusters, it was not used as the sole clustering method because it does not accurately provide cluster volume. Thus, it was combined with the isoconcentration surface method.

2.3 Simulation of Ni-Si-Mn Precipitation

Simulation can help provide additional insights into the mechanisms of precipitation behavior. In this work, we assume that the precipitation of the Ni-Si-Mn particles occurs due to the diffusion of the component species over long aging periods, during which regions occasionally reach a critical composition and particle nucleation occurs[21]. In order to establish whether segregation to the Cu-ferrite interface can significantly influence such a process, we must simulate this behavior using an approach that accounts for the random diffusion of these elements. FPKMC techniques have recently been employed by several authors to evaluate the propagation and self-organization of defects and species[49,52–55]. The main premise of this method is that diffusion-reaction processes can be efficiently simulated by considering the diffusing defects or species as Brownian particles. Each "walker" updates its position on the basis of a time-dependent Green's function, and the clock only advances from the motion of each subsequent walker outside of its "protected region", in which we assume there the walker does not interact with other walkers or the microstructure. Modeling diffusion in this way avoids calculations involving the motion of particles within each protected region. This is advantageous over molecular dynamics and lattice kinetic Monte Carlo methods, which can accurately predict atomic structure and morphology of the precipitates[11], but must consider every possible atomic "jump", which can be computationally expensive. It is important to point out that while this method does not account for other known influences on Ni-Si-Mn cluster precipitation, such as clustering at interfaces and the effects of species migration during spinodal decomposition, this method can evaluate the likely precipitation behavior for a region in bulk with a given composition, which allows us to predict for that composition the effects of Ni, Si, and Mn segregation to Cu precipitates.

Therefore, assuming the diffusive behavior of each species is approximately a three-dimensional random walk, the time at which a diffusing atom exits its protected region with width $r_{final} - r_{start}$, t_{FP}, can be expressed as:

$$t_{FP} = t_{\text{start}} + \frac{(r_{final} - r_{\text{start}})^2}{6D_{Species}M^2} \quad (4)$$

In this equation, t_{start} is the time at which the previous jump occurred, $D_{Species}$ is the diffusion coefficient of the atomic species, and M is a random number sampled from the standard normal distribution. Values of $D_{Species}$ were approximated from literature, as listed in Table 2.

Table 3: Diffusion coefficients of species

Parameter	Value	Source
D_{Ni}, D_{Si}, D_{Mn}	7.90x10-23 m^2/s	[56–60]
D_{Cu}	3.95x10-17 m^2/s	[61]

In order to implement this method for the simulation of Ni-Si-Mn precipitate formation, Ni, Si, Mn, and Cu species were allowed to migrate as though in a three-dimensional random walk. Several different reaction types were allowed in simulation. In the first, six Cu atoms in proximity would form a precipitate ($6Cu \rightarrow 6Cu_{Pr}$). While it is possible that additional Cu atoms in close proximity may be necessary for a stable Cu precipitate to form, preliminary simulations determined that Cu precipitates formed in similar number densities and volume fractions observed experimentally when the requirement for clustering was six Cu atoms. Since the main purpose of these simulations was to study the effect of Ni, Si, and Mn to the Cu precipitates and not the Cu precipitation kinetics, this was accepted as a reasonable facsimile for Cu precipitation. For the purpose of these simulations, it was assumed that nucleation of the Ni-Si-Mn particles would require critical concentrations of Ni, Si, and Mn. Therefore, in the second reaction, a critical composition of Ni, Si, and Mn would form a precipitate ($67Ni + 15Si + 29Mn \rightarrow 67Ni_{Pr} + 15Si_{Pr} + 29Mn_{Pr}$). This composition was selected in order to reflect the critical composition for nucleation identified by Matsukawa *et al*. [21] over a radius of 1.15 nm. Third, Ni, Si, and Mn were allowed to segregate to the ferrite/Cu interface (Ni/Si/Mn+ 20CuPr → NiCu/SiCu/MnCu + 20CuPr). In order to evaluate the impact of such an effect on Ni-Si-Mn precipitate formation, these reactions were disallowed in a second set of simulations. Finally, precipitated species could occasionally return to solid solution ($A_{Pr} \rightarrow A$) with an escape time ($t_{Exit} - t_{Start}$) sampled from an exponential probability distribution, as described in equation (5).

$$t_{Exit} - t_{Start} = -\beta_{Species} \ln(1 - r) \quad (5)$$

Here, r is a random number between 0 and 1. Atoms in a precipitate, therefore, can re-enter the solid solution after a mean passage of time $\beta_{Species}$, which allows for particle coarsening. Because we have no experimental data from which to base such a parameter, we have assumed $\beta_{Ni} = \beta_{Si} = \beta_{Mn} = 2300$ hours. Since from literature we believed that Cu diffusion was considerably more rapid than Ni, Si, or Mn diffusion, we assumed $\beta_{Cu} = 230$ hours. The simulations were run on a 57.4 nm x 57.4 nm x 57.4 nm microstructure for annealing periods of 1,500 and 10,000 hours at aging temperatures of 400 ˚C, 360 ˚C, and 330 ˚C. The compositions of Ni, Si, Mn, and Cu were selected to match compositions of each of the ferrite samples. At the end of each simulation, the final microstructure was evaluated for the presence of Ni, Si, Mn, and Cu rich regions.

3. RESULTS

3.1 Thermal aging-induced nanoscale precipitation

Thermal aging of duplex stainless steels and ferritic steels induces multiple microstructural changes within the ferrite phase: spinodal decomposition, precipitation of Ni-Si-Mn-rich particles, and precipitation of Cu-rich clusters[36]. Here we used STEM and primarily APT to investigate qualitatively and quantitatively how the presence of α/α' decomposition and Cu clusters affect the precipitation of Ni-Si-Mn particles. The STEM BF images in Figure 1 show the ferrite phase of the high Cu CF3 alloy (alloy A) aged at 400 ˚C for 1,500 hours (1a), 360 ˚C for 10,000 hours (1b), and 400 ˚C for 10,000 hours (1d), and the low Cu CF3 alloy (alloy B) aged at 360 ˚C (1c) and 400 ˚C (1e) for 10,000 hours. A fine distribution of nanoscale Ni-Si-Mn-rich particles are seen in each alloy at each condition with the alloys aged at 360 ˚C having smaller particles but a larger number density. At 10,000 hours at 400 ˚C, it appears the number density of precipitates in the low Cu alloy (1e) is less than the number density of precipitates in the high Cu alloy (1c). However, it is difficult to determine with high accuracy the particle volume fraction and number density, as well as it being difficult to ascertain any relationship between the particles and Cu clusters or spinodally decomposed interfaces. Further, determining the extent of precipitation in the early stages of thermal aging is even more problematic. This is particularly the case due to the projection issues of a 3D object with varying thickness onto a 2D plane in STEM imaging. Thus, APT analyses were used extensively to overcome these issues.

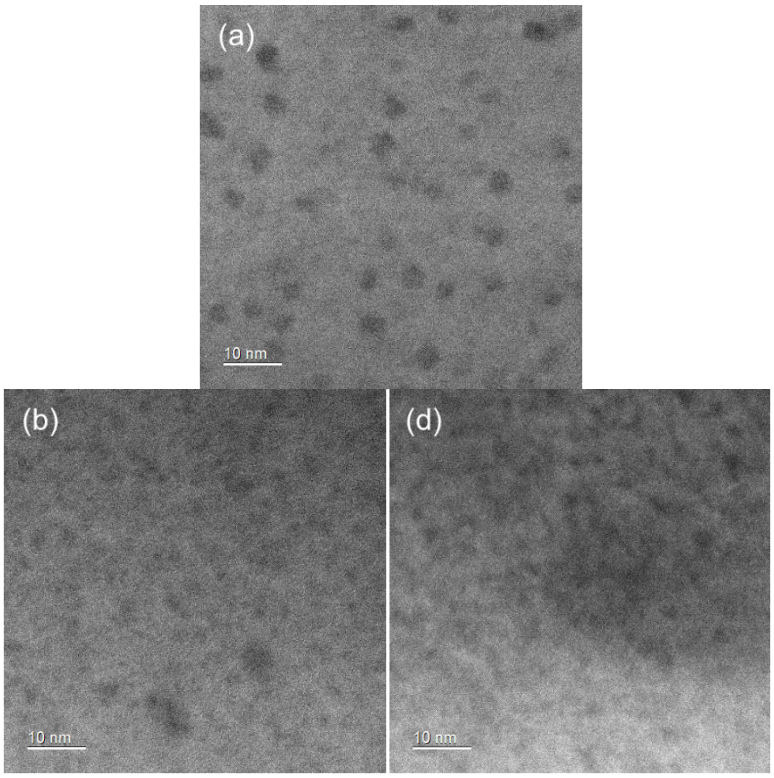

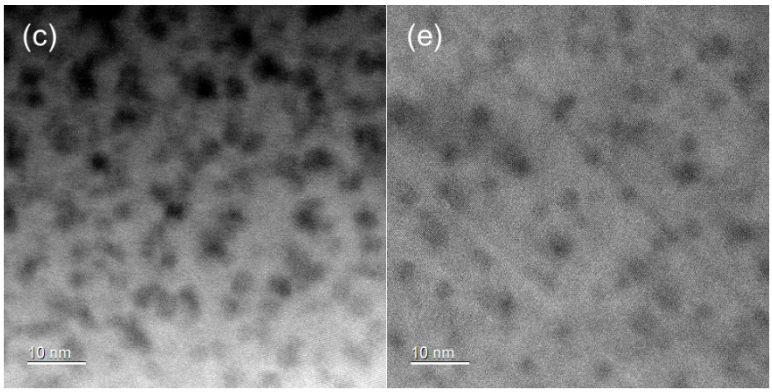

Figure 1: STEM BF images of the ferrite phase. (a) Alloy A aged for 1,500 hours at 400 ˚C; (b) Alloy A aged for 10,000 hours at 360 ˚C; (c) Alloy A aged for 10,000 hours at 400 ˚C; (d) Alloy B aged for 10,000 hours at 360 ˚C; and (e) Alloy B aged for 10,000 hours at 400 ˚C. Dark spots are the Ni-Si-Mn precipitates.

The extent of these microstructural changes as a function of aging temperature and time can be observed by the APT reconstructions shown in Figure 2 for the high Cu CF3 (alloy A). Similar plots of the low Cu CF3 alloy (alloy B) are shown in the supplemental material (Figures S1). These plots depict the spatial variation of elements within a 10nm thick slice of the reconstructions. Fe (not shown) and Cr separate from each other to greater levels with increasing aging temperature and time as shown in the point cloud reconstruction of Cr in column A. The G-phase forming elements – Ni, Si, and Mn – as shown in the point cloud reconstruction in column B and the 2D concentration plot in column C, group together at temperatures of 360 ˚C and 400 ˚C after 1,500 hours of aging, but after 10,000 hours of aging, they are also observed at 330 ˚C while increasing in number density up to 360 ˚C and size up to 400 ˚C. Both spinodal decomposition and G-phase precipitation are observed for both alloys (low and high Cu CF3) at 330 ˚C, but even more so at 360 ˚C and above. Column E shows the visualization of Ni-Si-Mn clusters found via the OPTICS-APT algorithm, and columns F and G show the visualization of Ni-Si-Mn clusters using 15% and 20% isosurfaces, respectively, as described in section 2.2. Comparing columns F and G with columns B, C, and E, the 15% isosurfaces (column F) match visually much better than the 20% isosurfaces, particularly at lower aging conditions such as 10,000 hours at 330 ˚C and 1,500 hours at 360 ˚C. Thus, 15% isosurfaces are used for quantifying Ni-Si-Mn clustering for all aging conditions. There is no Ni-Si-Mn and Cu clustering at 290 ˚C, so it was not included. However, with increased aging temperature, it is readily apparent that the Cu clusters, while initially overlapping with the Ni-Si-Mn clusters, become offset as appendages to the Ni-Si-Mn-rich precipitates based on the Cu 2D concentration plot and isosurfaces in columns D and H, respectively.

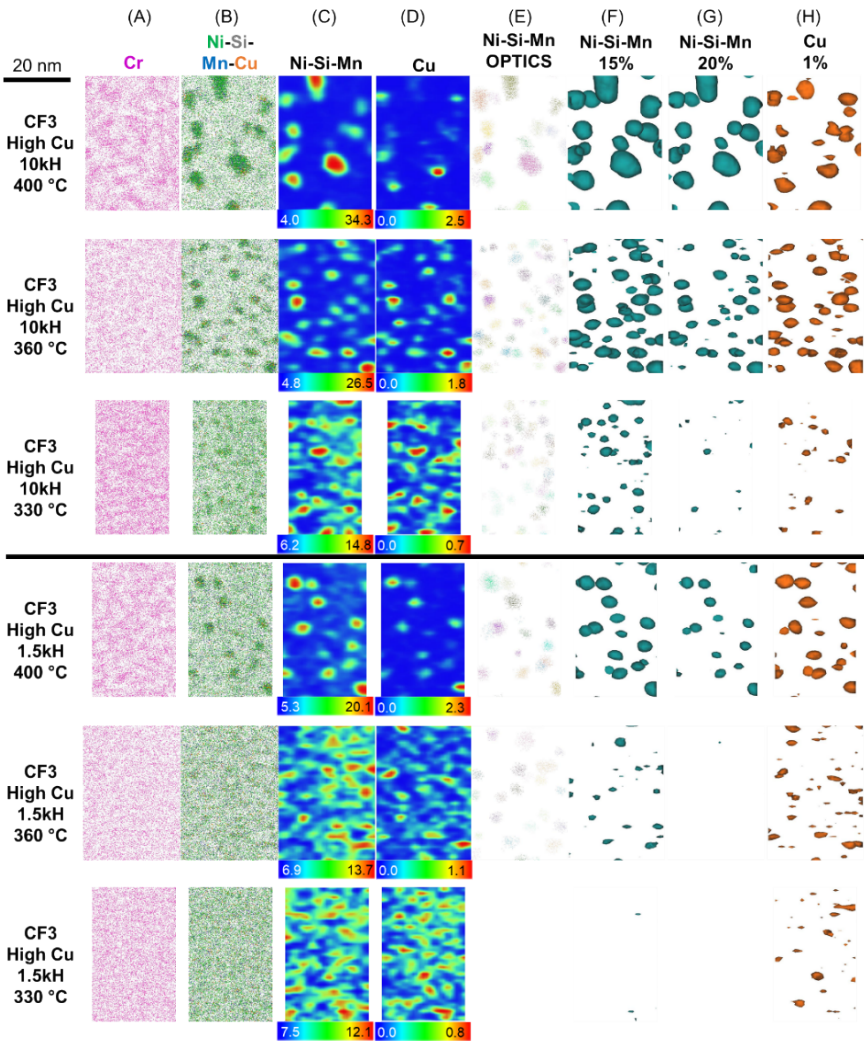

Figure 2: APT reconstructions for ferrite in Alloy A (High Cu CF3) aged for 10,000 and 1,500 hours at the three different aging temperatures. Regions are 10nm thick. (A, B) Point cloud reconstructions using Cr atoms and Ni-Si-Mn-Cu atoms, respectively. (C, D) 2D concentration contour plots for Ni-Si-Mn and Cu, respectively. (E) Ni-Si-Mn clusters identified by the OPTICS-APT algorithm. (F, G) Isoconcentration surfaces of Ni, Si, and Mn atoms at 15 at% and 20 at%, respectively. (H) Isoconcentration surfaces of Cu atoms at 1 at%.

The formation of Ni-Si-Mn/ Cu co-precipitates was further analyzed using 2D concentration contour plots of slices through Ni-Si-Mn and Cu precipitates in Figure 3 to determine exactly how these precipitates form as a function of thermal aging temperature. At 290 ˚C, Cu-rich clusters form; it is clear in Figure 3 that the cluster is enriched in Cu and slightly enriched in Ni though it is not centered on the Cu cluster, and there is no enrichment at all of Si or Mn. At 330 ˚C, Ni, Si, and Mn group together with the Cu to form a homogenous cluster. At 360 ˚C, Ni-Si-Mn-Cu particles grow and partially begin to form co-precipitates with Cu being rejected from the Ni-Si-Mn; in particular, Ni and Si are off-center from the Cu. Finally, at 400 ˚C, the Ni-Si-Mn precipitates have grown considerably, and the Cu clusters are attached as an appendage.

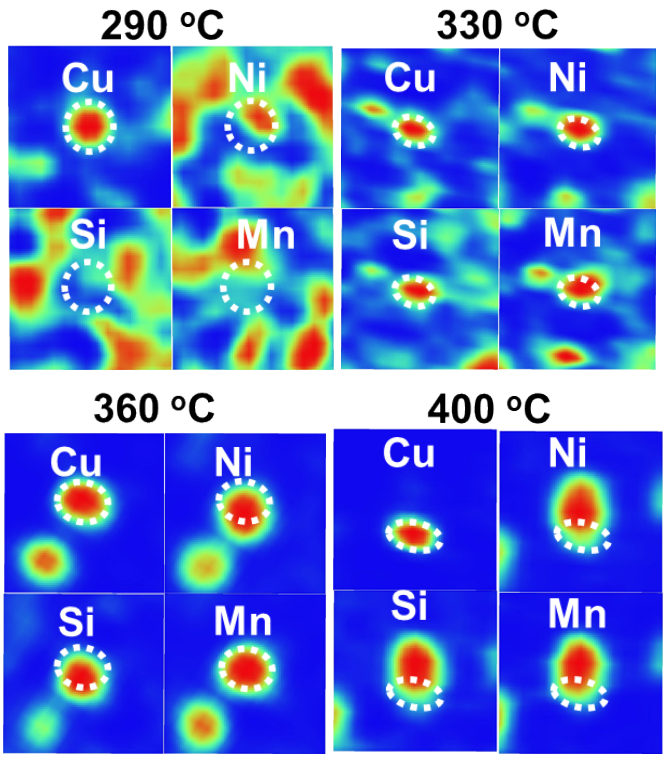

Figure 3: 2D concentration contour plots through either a Cu cluster or a Ni-Si-Mn/ Cu co-precipitate in the high Cu CF3 alloy (alloy A) after 10,000 hours of aging at each aging temperature. Dotted circles outline the location of the Cu-rich regions to help highlight if Cu is separate or incorporated with Ni-Si-Mn. Each panel region is 1nm thick and 15nmX15nm

3.2 Mechanistic understanding of precipitation-site competition

3.2.1 Experimental evaluation by quantitative atom probe tomography analyses

The large difference in Ni-Si-Mn and Cu clustering between the high and low Cu alloys were quantified using 15 at% Ni-Si-Mn and 1 at% Cu isosurfaces to determine the cluster volume fraction, number density, and average diameter as a function of equivalent aging time at 320 ˚C using an activation energy of 160 kJ/mol and alloy type, see Figure 4. For comparison, isosurface data for 20 at% and 25 at% are found in the supplemental material (Figures S4, S5, and S6.) In addition, the 15 at% isosurfaces also match well with analysis conducted using the OPTICS-APT algorithm[51], with comparison of them with respect to the solute fraction within the clusters found in the supplemental material (Figure S7).

There are two clear trends in the volume fraction and number density figures for both Ni-Si-Mn particles and Cu clusters. The CF3 alloys, which nominally have less carbon, have more overall clustering than the CF8 alloys. This is consistent with previous work by the authors that focused just on the high Cu alloys, where CF3 had more precipitation than their CF8 counterpart[36]. The other trend that is more pertinent to this study is that the high Cu (but lower Cr) alloys – both CF3 and CF8 – have more precipitation of both Ni-Si-Mn particles and Cu-rich clusters at elevated aging temperatures than their low Cu, higher Cr counterpart alloys. Clustering begins at an

equivalent aging time of ~2.0 years (using 160 kJ/mol) for all alloys, but it starts increasing at a greater rate in the high Cu alloys than in the low Cu alloys.

The trends are even more stark with respect to Cu-rich clusters. While the trend in volume fraction and number density of Cu clusters is similar to that of the Ni-Si-Mn particles with respect to the carbon concentration (CF3 vs CF8), the difference in Cu clustering is many times greater in the high Cu alloys than the low Cu alloys. The number density of Cu-rich clusters is at least an order of magnitude higher in the high Cu alloys during all equivalent aging times. This large disparity in Cu clustering is the primary reason for the disparity in the amount of precipitation of Ni-Si-Mn particles among the alloys, and not the level of spinodal decomposition, which we show has an inverse trend among the alloys.

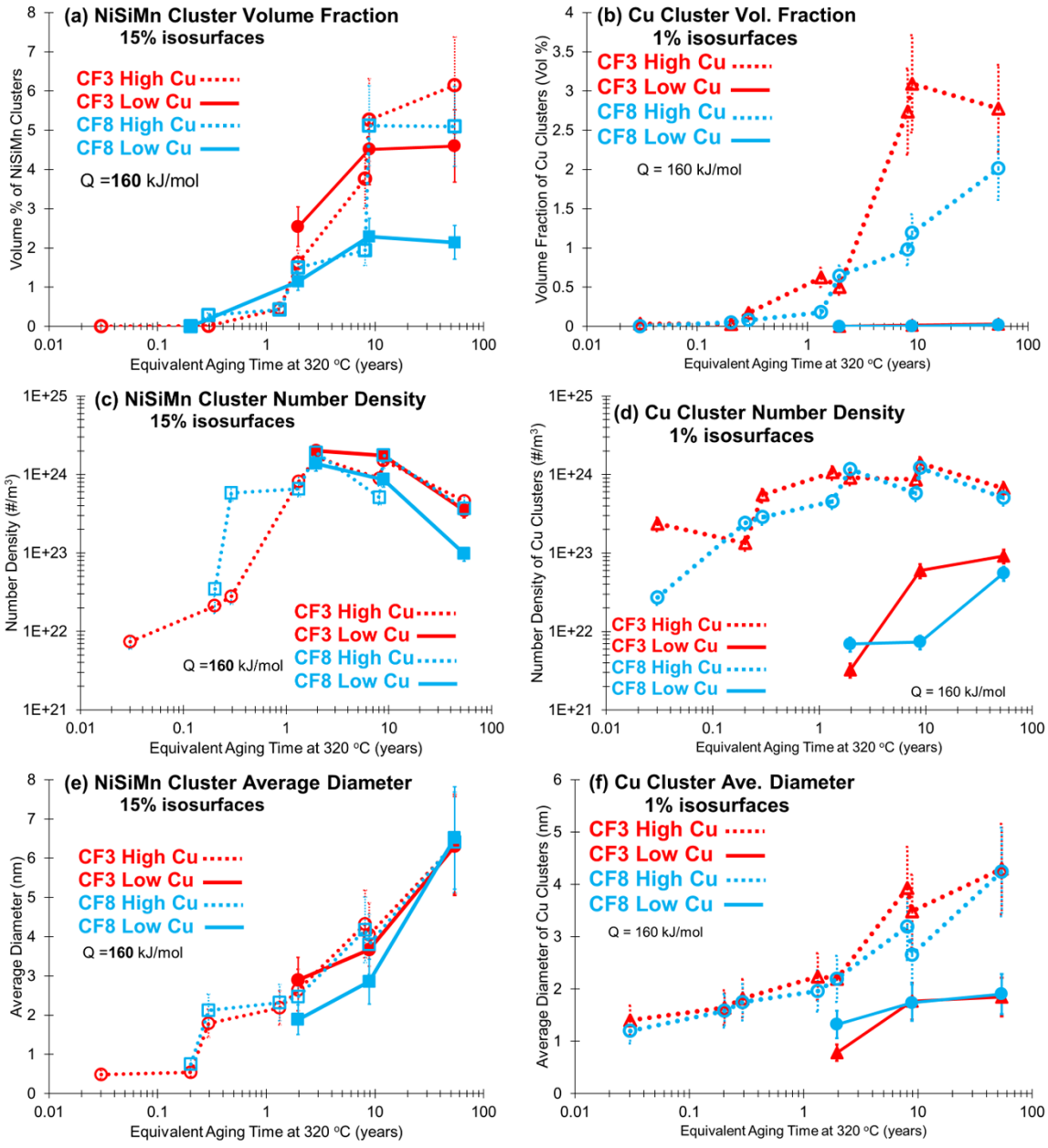

Figure 4: Ni-Si-Mn-rich cluster and Cu-rich cluster (a, b) volume fraction, (c, d) number density, and (e, f) average diameter using 15 at% isosurfaces for Ni-Si-Mn and 1 at% isosurfaces for Cu, respectively, for each alloy versus equivalent aging time at 320 ˚C using an activation energy of 160 kJ/mol

Radial distribution function (RDF) analyses further elucidate the relative importance of Cu clusters on Ni-Si-Mn precipitation as opposed to spinodal decomposition. The Cr-Cr radial distribution function plots in Figure 5 quantitatively show that the amplitude and wavelength of spinodal decomposition is much higher in the higher Cr and Ni alloys (low Cu) – alloys B and D. This is the case for both the CF3 and CF8 sets of alloys. Generally, the concentration of Cr, Ni, and Mo has the strongest effect on the degree of spinodal decomposition[25,35,36,62]. This is confirmed in the "X"-Cr RDF amplitude plots in Figure 6, where Cr has a strong attraction to other Cr atoms, and Ni has a strong repulsion to Cr atoms. The Cr-Cr and Ni-Cr plots show the higher Cr and Ni alloys (alloys B and D) have the greater attraction/ repulsion at all elevated aging temperatures. The interaction of Si and Mn with Cr is minor, but it is noticeable that there is an inflection point particularly in the Mn-Cr plot at an equivalent aging time of ~8.9 years for 160 kJ/mol at 320 ˚C (360 ˚C for 10,000 hours), which is at the same equivalent aging time that the Ni-Si-Mn-rich particles greatly increase in volume fraction (Figure 4). Of note, the alloys with higher extents of spinodal decomposition have less Ni-Si-Mn precipitation, see Figure 4.

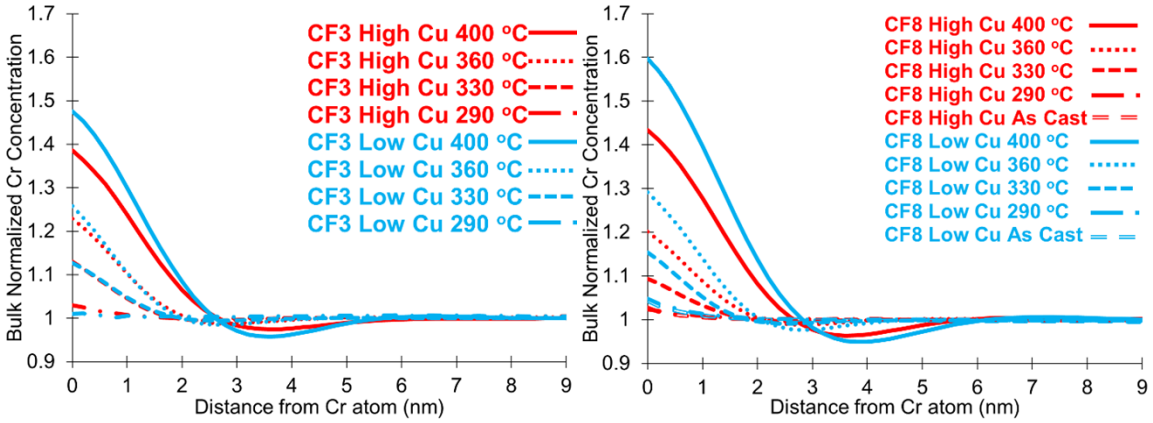

Figure 5: Radial distribution function plots of Cr atoms relative to Cr atoms for CF3 and CF8 high and low Cu alloys as a function of aging temperature after 10,000 hours of aging. RDF plots the bulk normalized concentration of an element vs distance from an atom of a given element (in this case Cr).

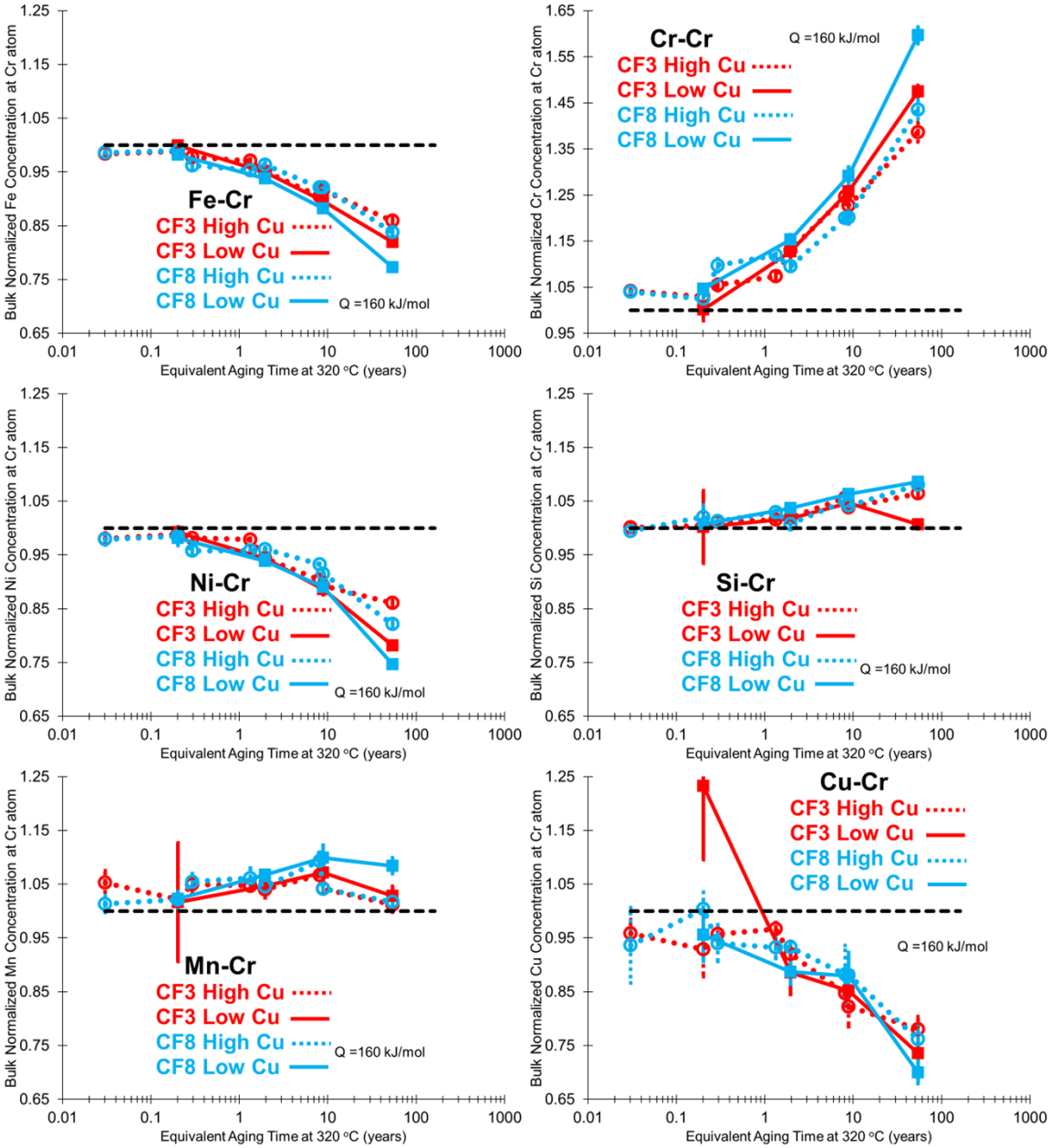

Figure 6: Bulk normalized concentration of Fe, Cr, Ni, Cu, Si, and Mn at an average Cr atom for each alloy as a function of equivalent aging time at 320 ˚C using an activation energy of 160 kJ/mol. The black dashed line at a value of 1 is there for reference; 1 equates to homogeneity.

Radial distribution function analysis of Ni atoms serves to determine elemental interactions that result in the precipitation and growth of Ni-Si-Mn G-phase particles as Ni constitutes more than half of G-phase ($Ni_{16}Si_7Mn_6$) – see supplemental material Figure S11 for approximate composition of Ni-Si-Mn clusters with aging. While the "wavelength" or distance between precipitates cannot be determined using RDF analyses, the RDF "amplitude" or bulk normalized concentration at Ni atoms does show the interactions each element has with Ni. As established in Figure 7, Ni segregates away from Fe and Cr with increasing aging temperature, while at the same time it

correlates with Ni, Si, Mn, and Cu. The high Cu alloys and low C alloys have the most segregation compared to the low Cu alloys and high Cu alloys. The big jump in concentration of Ni, Cu, Si, and Mn near Ni atoms occurs from an equivalent aging time at 320 ˚C using 160 kJ/mol of ~2.0 years to an aging time of ~8.9 years. This corresponds with the increase in Ni-Si-Mn cluster volume fraction in all alloys in Figure 4. These jumps are largest in Cu and Mn relative to Ni, whereas Ni and Si are more muted. The change in concentration of Cu near Ni atoms (Cu-Ni) with aging temperature/ time has by far the greatest difference between the low and high Cu alloys compared to the other elements relative to Ni atoms. This information, combined with the precipitation data in Figure 4, shows that the larger Cu concentration likely enhances the precipitation of the Ni-Si-Mn precipitates.

To further show that the presence of additional Cu promotes precipitation of Ni-Si-Mn precipitates, RDF analysis relative to Cu atoms of the four alloys is used, see supplemental material Figure S12. The RDF amplitude of elements relative to Cu follows similar trends to those relative to Ni, but to a greater degree with respect to Ni, Mn, and especially Cu. The high Cu alloys and CF3 alloys have the most segregation compared to the low Cu alloys and CF8 alloys.

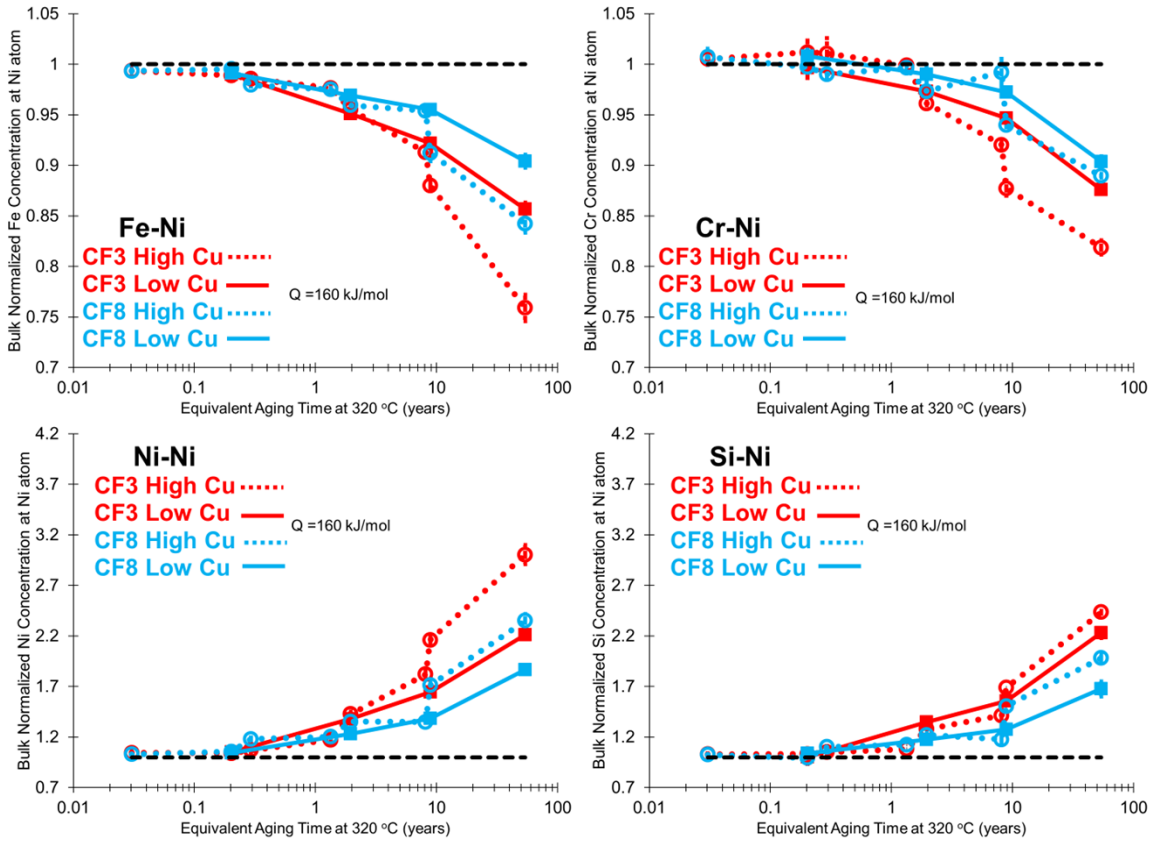

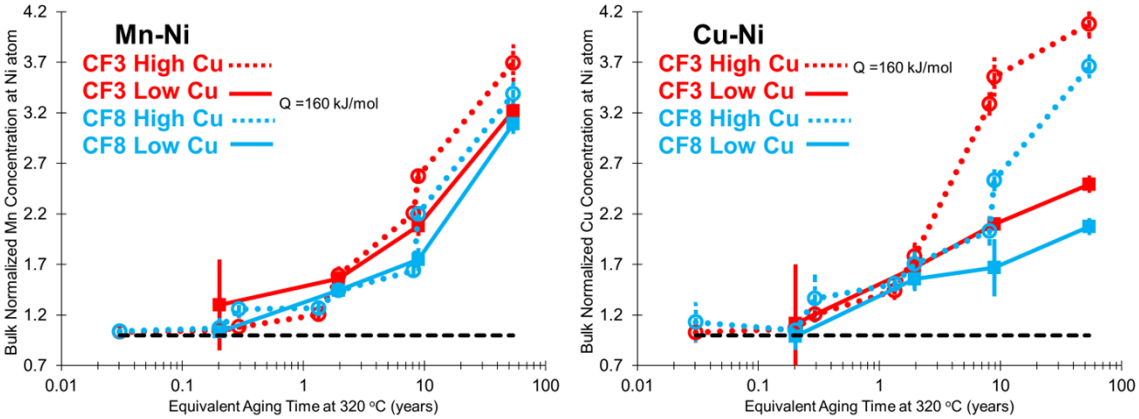

Figure 7: Bulk normalized concentration of Fe, Cr, Ni, Cu, Si and Mn at an average Ni atom for each alloy as a function of equivalent aging time at 320 ˚C using an activation energy of 160 kJ/mol. The black dashed line at a value of 1 is there for reference; 1 equates to homogeneity.

3.2.2 Importance of species segregation modeled by first-passage kinetic Monte Carlo simulation

FPKMC simulations of aging indicate that Cu promotes the formation of Ni-Si-Mn precipitates. It can be seen in Figure 8 of alloys A and B (C and D in supplemental material Figure S16) that when Cu content is elevated to 0.22% from 0.06%, the predicted number density and volume fraction of Ni-Si-Mn precipitates increases significantly. It is noticeable in our simulations that Cu clusters appear to increase in number density with increasing Cu content. The volume fraction of Cu clusters also increases significantly with increased Cu content. This is in reasonable agreement with the experimental APT results. Additionally, Ni-Si-Mn-rich clusters do not form when Ni, Si, and Mn have no preference for segregation to the Cu-ferrite interface. This suggests that this segregation has an influence on the formation of the Ni-Si-Mn particles, and that the Cu-ferrite interface is a very strong interface for precipitation. Future simulation work will more closely examine the influence of the segregation of each individual species on Ni-Si-Mn cluster formation.

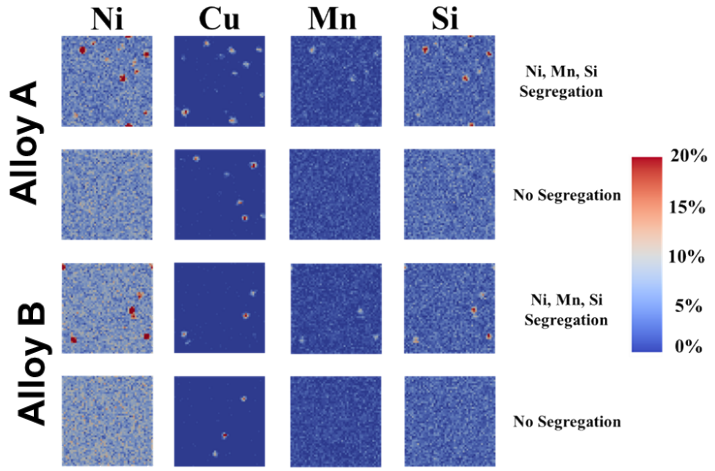

Figure 8: Composition of ferrite in alloys A and B after 10,000 hours of aging at 400 ˚C, as simulated using the FPKMC method, either allowing or disallowing Ni/Cu segregation.

It is visually apparent that from FPKMC simulation that Ni-Si-Mn cluster formation increases considerably with increasing temperature. Figure 9 for alloys A and B (supplemental material Figures S16 and S17 for alloys C and D), which shows the content of each species after 10,000 hours, reveal a considerable amount of segregation of Ni, Si, and Mn around the Cu precipitates at 400 ˚C, as shown in Figure 8. This segregation around Cu clusters is considerably less at 330 ˚C, as expected when comparing to the APT data in Figures 2 and 3. The number of Cu precipitates present also appears to have decreased, especially in alloy B, where Cu content was lower. This is consistent with measurements of Cu volume fraction in Figure 4. An analysis of the Ni-Si-Mn cluster volume fractions, number densities, and diameters, shown in supplemental material (Figures S18 and S19) shows similar trends to those that have been calculated from APT measurements. However, the extent of precipitation at 330 ºC and 360 ºC appears to be somewhat less than that observed by APT. This suggests that the effects of spinodal decomposition, which would result in additional sites for Ni-Si-Mn cluster precipitation and addition migration of Cu, Ni, Si, and Mn, may have a stronger effect on the precipitation behavior at these temperatures.

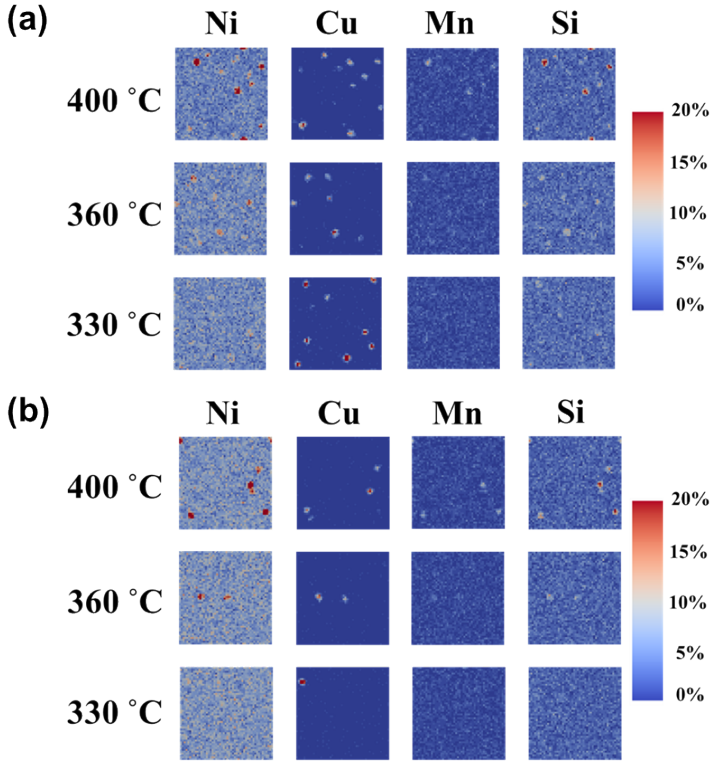

Figure 9. Composition of ferrite in (a) alloy A and (b) alloy B after 10,000 hours of aging at 330 ˚C, 360 ˚C, and 400 ˚C, as simulated using the FPKMC method, allowing segregation to Cu precipitates.

4. DISCUSSION

Complex, multicomponent alloys like these duplex stainless steels allowed us to investigate interdependent mechanisms for precipitation. Using duplex stainless steels with modified composition along with APT analysis of microstructure and FPKMC simulation, we were able to determine the chemical and structural characteristics that promote or hinder precipitation of Ni-Si-Mn-rich particles in the ferrite phase of duplex stainless steels during thermal aging. Ni-Si-Mn

precipitation and co-precipitation with Cu is of great interest in RPV and ferritic steels as it is seen as a detriment to properties[63]. However, the relative influence of small amounts of Cu on precipitation in high Cr and high Ni steels is not fully understood. Two competing explanations from prior research in duplex steels and ferritic/ RPV steels were considered: precipitation at the interface of Fe-rich α and Cr-rich α' that forms during spinodal decomposition[64] and co-precipitation on Cu-rich clusters[11]. We showed that both do take place, but that the effect of Cu is much more pronounced, and the presence of even a small concentration of Cu serves as a large driving force for precipitation of Ni-Si-Mn precipitates. Some of the key findings include:

- Cu clusters appear to form first at the early stages of spinodally decomposed Fe-Cr boundaries, even at 290 ˚C after 1,500 and 10,000 hours of aging.
- Ni and Mn atoms are the first to segregate to the Cu clusters, followed by Si atoms with increasing aging temperature and time.
- As the Ni-Si-Mn particles grow, the Ni, Si, and Mn segregate from Cu atoms but remain in contact as co-precipitates.
- Even in the low Cu alloys, there is some Cu enrichment in the Ni-Si-Mn particles and/or Cu co-precipitation with Ni-Si-Mn particles.

The α/α' interface formed during spinodal decomposition only moderately promotes precipitate nucleation. Despite forming in local Cr and Fe concentration minima and having similar Ni, Si, and Mn concentrations, the additional Cu in the higher Cu alloys serves as the best seed for nucleation of more Ni-Si-Mn precipitates compared to the low Cu alloys. If the α/α' interface served as a better location for precipitation of Ni-Si-Mn precipitates, the higher Cr alloys B and D would have more precipitation, but the opposite is the case. Future research on high Cu, higher Cr alloys and low Cu, lower Cr alloys is needed to fully deconvolute these effects, but the relatively small difference in Cr concentration among the alloys and the prevalence of Ni-Si-Mn/ Cu co-precipitates in low Cr RPV steels lends strong credence to our conclusions.

In the higher Cu alloys, Cu is the first to form clusters after only 1,500 hours of annealing at 290 ˚C. This behavior is reasonable to expect, as Cu is strongly immiscible with Fe and Cr, among many other elements[28,65]. At 330 ˚C and higher aging temperatures, Ni, Mn, and increasingly Cu segregate out of the Fe and Cr rich regions to the boundary between the two. Especially at low aging temperatures, this boundary is quite diffuse as seen in Figure 2 and the 2D concentration contour plots in the supplemental material (Figure S3) and previous research[35,36,66], as even in the as-cast state, there is some minor variation in local Fe and Cr content. These variations grow with increased aging temperature and aging time. The boundary between Fe and Cr could serve as a pathway for enhanced diffusion of other elements[25,61], just as grain boundaries and dislocations enhance localized diffusion[67]. The emission of other atoms (Ni, Mn, Cu, and Si) increases with increasing aging temperature as the Fe and Cr rich regions become purer and the interface between the two regions becomes sharper. Interestingly, as depicted in in the Cr-based RDFs in Figure 6, alloys B and D, which have more Ni and Cr but less Cu, have Ni segregated more from Cr. However, this increased segregation to the α/α' interface doesn't lead to more precipitation as the higher Cr alloys have less precipitation. The "web-like" interconnected α/α' interfaces may act as high diffusivity pathways much like pipe diffusion in highly worked materials with high dislocation densities[62,67], but because the α/α' interface is coherent, particularly in the early stages of decomposition, there is a lack of free volume and driving force

available to encourage precipitation. On the other hand, the semi-coherent and high energy interface between Cu and Fe or Cu and Cr acts as a good location for atoms to segregate towards and form precipitates[11].

The presence of Cu clusters of even a few atoms attracts the Ni-Si-Mn elements to form homogeneous Ni-Si-Mn-Cu particles, as evidenced by the FPKMC simulation presented in Figures 8-9. Without this attraction, the precipitation of Ni-Si-Mn does not take place in the simulation. While the effect of Cr is not considered in the simulation, the need for an attraction between Ni and Cu for precipitation of Ni-Si-Mn strongly supports the APT evidence of high Cu alloys having a larger volume fraction of Ni-Si-Mn precipitates. Consistent with research on Ni-Al/ Cu co-precipitates in an Fe matrix[68], Cu forms clusters with Ni or acts as a seed for Ni (and other elements) to segregate depending on the Ni:Cu ratio. As the nanoparticles grow in both cases of high or low Ni:Cu ratio, the Cu atoms are rejected towards the particle surface forming adjacent Cu-rich clusters[69,70]. The Cu clusters remain attached to the Ni-Si-Mn precipitate to limit the interfacial area of the high-energy Cu-Fe interface[11]. This work here further provides strong evidence that Cu, even at relatively low concentrations, enhances precipitation of Ni-Si-Mn whether it acts as a surface for precipitation or as an increase in the driving force for precipitation. Even with increased Ni, Si, and Mn content in these steels, where the ease of precipitation of Ni-Si-Mn particles would be suspected to be high, the mere presence of Cu greatly enhances precipitation of Ni-Si-Mn particles. The interface between Cu and the matrix acts in a similar way to that of irradiated materials providing locations for precipitation via dislocation loops and grain boundaries[13]. The presence of a higher Cu content increases the driving force for precipitation of Ni-Si-Mn particles, which form at earlier stages of aging than the low Cu alloys, see Figure 4. Thus, as seen in irradiated environments[71], the so-called “late blooming phase” actually precipitates relatively early, even in a thermal aging, non-irradiated environment. The presence of Cu accelerates this precipitation.

While in our previous work, we stated that Cu initially incorporated into the Ni-rich particles[36], this may be the case only at elevated aging temperatures of 330 ˚C and higher. At 290 ˚C after both 1,500 and 10,000 hours of aging, only small Cu clusters are found, and these generally are not enriched in Ni, Si, or Mn, see Figure 3. However, at or above 330 ˚C after 1,500 or 10,000 hours of aging, the Cu clusters have enrichment in Ni, Si, and Mn, or are attached to Ni-Si-Mn particles. Thus, precipitation at or below aging temperatures of 290 ˚C may be demonstrative of either the early stages of precipitation seen at higher aging temperatures or of a different mechanism for precipitation than aging at temperatures between 330 ˚C and 400 ˚C. This is consistent with previous research[25,62], where the activation energy for precipitation and spinodal decomposition changes in the temperature range of 300-325 ˚C. This may present issues with using accelerated aging at temperatures of 330 ˚C or higher to predict performance at or around 290 ˚C or less. At these low aging temperatures, Cu may precipitate out first and act as a seed for nucleation of Ni-Si-Mn precipitates, more in the fashion of low Ni:Cu ratio alloys that have Ni and Cu precipitating as one together[68]. Nonetheless, additional Cu enhances the precipitation of Ni-Si-Mn, no matter what the actual mechanism is. Further research on a longer-term aging is needed to assess the two potential mechanisms above or below 330 ˚C.

The importance of this research on mechanical behavior is well evident. Several studies have pointed to the relative importance of Ni-Si-Mn precipitation on the hardening of the ferrite phase

during aging or irradiation[23–25]. With a high number density and large volume fraction, it is clear that these precipitates act as obstacles for dislocations. While reducing Cr will reduce the extent of spinodal decomposition, which causes hardening on its own, it is not very effective in reducing the precipitation of Ni-Si-Mn particles which recent research has indicated may have a larger impact on hardening than spinodal decomposition[25]. Thus, reducing the Cu concentration in these alloys could go a long way to reducing the thermal aging-induced hardening.

With this work, predictive models can undergo development for the long-term capabilities of these alloys at service temperatures. In upcoming work, the present study will be combined with microstructural characterization on the evolution of the austenite-ferrite phase boundary during thermal aging where the importance Cu concentration may impact the precipitation of Ni-Si-Mn and the size of the precipitate denuded zone[72]. The findings from these studies will enhance understanding of precipitation mechanisms and their relationship on materials properties during thermal aging and/or radiation.

5. CONCLUSIONS

Precipitation mechanisms and the dependence on heterogeneous nucleation during thermal aging of high Cr and high Ni duplex stainless steels were investigated in detail. The relative influences of Cr and Cu on precipitation of Ni-Si-Mn particles were compared. Knowing these precipitation mechanisms and their dependencies are of utmost importance for predicting thermal aging-induced degradation in duplex stainless steels and ferritic steels. In this work, we characterized four cast austenitic stainless steels – two CF3 and two CF8 alloys – aged for 1,500 and 10,000 hours at 290, 330, 360, and 400 ˚C. The sets of alloys were split further into two subsets of alloys: higher Cu and lower Cr compared to lower Cu and higher Cr. The major takeaways are:

- Alloys with an elevated Cu concentration (>0.2at%) have more precipitation of Ni-Si-Mn particles than alloys with reduced Cu concentration but higher Cr and Ni concentrations.
- Spinodal decomposition results in a diffusion network where Cu, Ni, Mn, and Si can diffuse more efficiently; however, this interface between Fe-rich α and Cr-rich α' does not necessarily encourage Ni-Mn-Si precipitation.
- Cu has a profound effect on precipitation because it is strongly immiscible in Fe and has a high energy interface with Fe.
- In alloys with elevated Cu, Cu forms small clusters at aging temperatures of 290 ˚C and is not enriched in other elements. At an aging temperature of 330 ˚C, these Cu clusters are enriched in Ni, Si, and Mn, and begin to form co-precipitates of Cu clusters attached to Ni-Si-Mn particles. At the longest equivalent aging times, all sets of clusters are co-precipitates.
- In low Cu alloys, Ni-Si-Mn precipitates form to a smaller extent at each aging temperature. At an aging temperature of 330 ˚C, Ni-Si-Mn particles are enriched with some Cu, and at higher aging temperatures, either Ni-Si-Mn particles are enriched in Cu or form co-precipitates with Cu clusters. The presence of Cu in or attached to these clusters highlights the importance of Cu on the kinetics of precipitation of Ni-Si-Mn particles.

ACKNOWLEDGEMENTS

This research was partly sponsored by the Laboratory Directed Research and Development Program of Oak Ridge National Laboratory, managed by UT-Battelle, LLC, for the U. S. Department of Energy under contract number DE-AC05-00OR22725. The analysis was based upon the result of experiment research supported by the LWR Sustainability Program for the U.S. Department of Energy, Office of Nuclear Energy (LW-18OR040215) at Pacific Northwest National Laboratory (PNNL) operated by Battelle Memorial Institute for the U.S. Department of Energy under Contract No. DEAC05-76RL01830. APT was performed at PNNL's Environmental Molecular Sciences Laboratory, a Department of Energy - Office of Biological & Environmental Research national scientific user facility. Electron microscopy was performed at PNNL's Radiological Microscopy Suite at the Radiochemical Processing Laboratory using PNNL's Institutional Microscopy Tools. The authors also thank Dr. Shenyang Hu at Pacific Northwest National Laboratory, for numerous fruitful discussions regarding the computational modeling of Ni-Si-Mn cluster precipitation.

DATA AVAILABILITY

The raw/processed data required to reproduce these findings cannot be shared at this time as the data also forms part of an ongoing study.

REFERENCES

[1] S. Shu, N. Almirall, P.B. Wells, T. Yamamoto, G.R. Odette, D.D. Morgan, Precipitation in Fe-Cu and Fe-Cu-Mn model alloys under irradiation: Dose rate effects, Acta Mater. 157 (2018) 72–82. https://doi.org/https://doi.org/10.1016/j.actamat.2018.07.017.

[2] J.E. Westraadt, E.J. Olivier, J.H. Neethling, P. Hedström, J. Odqvist, X. Xu, A. Steuwer, A high-resolution analytical scanning transmission electron microscopy study of the early stages of spinodal decomposition in binary Fe–Cr, Mater. Charact. 109 (2015) 216–221. https://doi.org/https://doi.org/10.1016/j.matchar.2015.10.001.

[3] M. Hättestrand, J.-O. Nilsson, K. Stiller, P. Liu, M. Andersson, Precipitation hardening in a 12%Cr–9%Ni–4%Mo–2%Cu stainless steel, Acta Mater. 52 (2004) 1023–1037. https://doi.org/https://doi.org/10.1016/j.actamat.2003.10.048.

[4] K.L. Murty, K. Ramaswamy, 1 - Overview of ageing and degradation issues in light water reactors (LWRs), in: K.L. Murty (Ed.), Mater. Ageing Degrad. Light Water React., Woodhead Publishing, 2013: pp. 3–69. https://doi.org/https://doi.org/10.1533/9780857097453.1.3.

[5] T.S. Byun, J.T. Busby, Light Water Reactor Sustainability Cast Stainless Steel Aging Research Plan, 2012.

[6] J.D. Tucker, M.K. Miller, G.A. Young, Assessment of thermal embrittlement in duplex stainless steels 2003 and 2205 for nuclear power applications, Acta Mater. 87 (2015) 15–24. https://doi.org/https://doi.org/10.1016/j.actamat.2014.12.012.

[7] H.-H. Lu, H.-K. Guo, Y. Luo, Z.-G. Liu, W.-Q. Li, J.-C. Li, W. Liang, Microstructural evolution, precipitation and mechanical properties of hot rolled 27Cr-4Mo-2Ni ferritic steel during 800 °C aging, Mater. Des. 160 (2018) 999–1009. https://doi.org/https://doi.org/10.1016/j.matdes.2018.10.039.

[8] P.D. Styman, J.M. Hyde, K. Wilford, A. Morley, G.D.W. Smith, Precipitation in long term thermally aged high copper, high nickel model RPV steel welds, Prog. Nucl. Energy. 57

(2012) 86–92. https://doi.org/https://doi.org/10.1016/j.pnucene.2011.10.010.
[9] S. Mohanty, N.P. Gurao, P. Padaikathan, K. Biswas, Ageing behaviour of equiatomic consolidated Al20Co20Cu20Ni20Zn20 high entropy alloy, Mater. Charact. 129 (2017) 127–134. https://doi.org/https://doi.org/10.1016/j.matchar.2017.04.011.
[10] J.-H. Ke, H. Ke, G.R. Odette, D. Morgan, Cluster dynamics modeling of Mn-Ni-Si precipitates in ferritic-martensitic steel under irradiation, J. Nucl. Mater. 498 (2018) 83–88. https://doi.org/https://doi.org/10.1016/j.jnucmat.2017.10.008.
[11] S. Shu, P.B. Wells, N. Almirall, G.R. Odette, D.D. Morgan, Thermodynamics and kinetics of core-shell versus appendage co-precipitation morphologies: An example in the Fe-Cu-Mn-Ni-Si system, Acta Mater. 157 (2018) 298–306. https://doi.org/https://doi.org/10.1016/j.actamat.2018.07.037.
[12] J.M. Hyde, G. Sha, E.A. Marquis, A. Morley, K.B. Wilford, T.J. Williams, A comparison of the structure of solute clusters formed during thermal ageing and irradiation, Ultramicroscopy. 111 (2011) 664–671. https://doi.org/https://doi.org/10.1016/j.ultramic.2010.12.030.
[13] K. Lindgren, M. Boåsen, K. Stiller, P. Efsing, M. Thuvander, Cluster formation in in-service thermally aged pressurizer welds, J. Nucl. Mater. 504 (2018) 23–28. https://doi.org/https://doi.org/10.1016/j.jnucmat.2018.03.017.
[14] V. Kuksenko, C. Pareige, P. Pareige, Cr precipitation in neutron irradiated industrial purity Fe–Cr model alloys, J. Nucl. Mater. 432 (2013) 160–165. https://doi.org/https://doi.org/10.1016/j.jnucmat.2012.07.021.
[15] P.D. Styman, J.M. Hyde, K. Wilford, D. Parfitt, N. Riddle, G.D.W. Smith, Characterisation of interfacial segregation to Cu-enriched precipitates in two thermally aged reactor pressure vessel steel welds, Ultramicroscopy. 159 (2015) 292–298. https://doi.org/https://doi.org/10.1016/j.ultramic.2015.05.013.
[16] P.D. Styman, J.M. Hyde, A. Morley, K. Wilford, N. Riddle, G.D.W. Smith, The effect of Ni on the microstructural evolution of high Cu reactor pressure vessel steel welds after thermal ageing for up to 100,000 h, Mater. Sci. Eng. A. 736 (2018) 111–119. https://doi.org/https://doi.org/10.1016/j.msea.2018.08.063.
[17] D. Isheim, M.S. Gagliano, M.E. Fine, D.N. Seidman, Interfacial segregation at Cu-rich precipitates in a high-strength low-carbon steel studied on a sub-nanometer scale, Acta Mater. 54 (2006) 841–849. https://doi.org/https://doi.org/10.1016/j.actamat.2005.10.023.
[18] Z. Jiao, V. Shankar, G.S. Was, Phase stability in proton and heavy ion irradiated ferritic–martensitic alloys, J. Nucl. Mater. 419 (2011) 52–62. https://doi.org/https://doi.org/10.1016/j.jnucmat.2011.08.020.
[19] W. Guo, D.A. Garfinkel, J.D. Tucker, D. Haley, G.A. Young, J.D. Poplawsky, An atom probe perspective on phase separation and precipitation in duplex stainless steels, Nanotechnology. 27 (2016) 254004. https://doi.org/10.1088/0957-4484/27/25/254004.
[20] X. Cao, P. Zhu, W. Wang, T. Liu, Y. Lu, T. Shoji, Precipitation behavior of stainless steel weld overlay cladding exposed to a long-term thermal aging, Mater. Charact. 137 (2018) 77–83. https://doi.org/https://doi.org/10.1016/j.matchar.2018.01.018.
[21] Y. Matsukawa, T. Takeuchi, Y. Kakubo, T. Suzudo, H. Watanabe, H. Abe, T. Toyama, Y. Nagai, The two-step nucleation of G-phase in ferrite, Acta Mater. 116 (2016) 104–113. https://doi.org/https://doi.org/10.1016/j.actamat.2016.06.013.
[22] J. Emo, C. Pareige, S. Saillet, C. Domain, P. Pareige, Kinetics of secondary phase precipitation during spinodal decomposition in duplex stainless steels: A kinetic Monte

Carlo model – Comparison with atom probe tomography experiments, J. Nucl. Mater. 451 (2014) 361–365. https://doi.org/https://doi.org/10.1016/j.jnucmat.2014.04.025.
[23] S.C. Schwarm, S. Mburu, R.P. Kolli, D.E. Perea, S. Ankem, Effects of long-term thermal aging on bulk and local mechanical behavior of ferritic-austenitic duplex stainless steels, Mater. Sci. Eng. A. 720 (2018) 130–139. https://doi.org/https://doi.org/10.1016/j.msea.2018.02.058.
[24] Q. Zhang, A.S.S. Singaravelu, Y. Zhao, T. Jing, N. Chawla, Mechanical properties of a thermally-aged cast duplex stainless steel by nanoindentation and micropillar compression, Mater. Sci. Eng. A. 743 (2019) 520–528. https://doi.org/https://doi.org/10.1016/j.msea.2018.11.112.
[25] R. Badyka, G. Monnet, S. Saillet, C. Domain, C. Pareige, Quantification of hardening contribution of G-Phase precipitation and spinodal decomposition in aged duplex stainless steel: APT analysis and micro-hardness measurements, J. Nucl. Mater. 514 (2019) 266–275. https://doi.org/https://doi.org/10.1016/j.jnucmat.2018.12.002.
[26] F. Bergner, C. Pareige, M. Hernández-Mayoral, L. Malerba, C. Heintze, Application of a three-feature dispersed-barrier hardening model to neutron-irradiated Fe–Cr model alloys, J. Nucl. Mater. 448 (2014) 96–102. https://doi.org/https://doi.org/10.1016/j.jnucmat.2014.01.024.
[27] G. Monnet, Multiscale modeling of precipitation hardening: Application to the Fe–Cr alloys, Acta Mater. 95 (2015) 302–311. https://doi.org/https://doi.org/10.1016/j.actamat.2015.05.043.
[28] P. Franke, D. Neuschutz, Binary Systems. Part 2: Elements and Binary Systems B-C to Cr-Zr: Cr-Fe, in: Landolt-Bornstein - Gr. IV Phys. Chem., Springer Books, n.d.
[29] P. Hedström, F. Huyan, J. Zhou, S. Wessman, M. Thuvander, J. Odqvist, The 475°C embrittlement in Fe–20Cr and Fe–20Cr–X (X=Ni, Cu, Mn) alloys studied by mechanical testing and atom probe tomography, Mater. Sci. Eng. A. 574 (2013) 123–129. https://doi.org/https://doi.org/10.1016/j.msea.2013.03.016.
[30] H.D. Solomon, L.M. Levinson, Mössbauer effect study of '475°c embrittlement' of duplex and ferritic stainless steels, Acta Metall. 26 (1978) 429–442. https://doi.org/https://doi.org/10.1016/0001-6160(78)90169-4.
[31] J.E. Brown, G.D.W. Smith, Atom probe studies of spinodal processes in duplex stainless steels and single- and dual-phase Fe-Cr-Ni alloys, Surf. Sci. 246 (1991) 285–291. https://doi.org/https://doi.org/10.1016/0039-6028(91)90428-U.
[32] C. Pareige, S. Novy, S. Saillet, P. Pareige, Study of phase transformation and mechanical properties evolution of duplex stainless steels after long term thermal ageing (>20years), J. Nucl. Mater. 411 (2011) 90–96. https://doi.org/https://doi.org/10.1016/j.jnucmat.2011.01.036.
[33] F. Danoix, P. Auger, D. Blavette, An atom-probe investigation of some correlated phase transformations in Cr, Ni, Mo containing supersaturated ferrites, Surf. Sci. 266 (1992) 364–369. https://doi.org/https://doi.org/10.1016/0039-6028(92)91047-F.
[34] A. MATEO, L. LLANES, M. ANGLADA, A. REDJAIMIA, G. METAUER, Characterization of the intermetallic G-phase in an AISI 329 duplex stainless steel, J. Mater. Sci. 32 (1997) 4533–4540. https://doi.org/10.1023/A:1018669217124.
[35] T.G. Lach, T.S. Byun, K.J. Leonard, Mechanical property degradation and microstructural evolution of cast austenitic stainless steels under short-term thermal aging, J. Nucl. Mater. 497 (2017) 139–153. https://doi.org/https://doi.org/10.1016/j.jnucmat.2017.07.059.

[36] T.G. Lach, A. Devaraj, K.J. Leonard, T.S. Byun, Co-dependent microstructural evolution pathways in metastable δ-ferrite in cast austenitic stainless steels during thermal aging, J. Nucl. Mater. 510 (2018). https://doi.org/10.1016/j.jnucmat.2018.08.038.
[37] T.S. Byun, Y. Yang, N.R. Overman, J.T. Busby, Thermal Aging Phenomena in Cast Duplex Stainless Steels, JOM. 68 (2016) 507–516. https://doi.org/10.1007/s11837-015-1709-9.
[38] S.J. Zinkle, G.S. Was, Materials challenges in nuclear energy, Acta Mater. 61 (2013) 735–758. https://doi.org/https://doi.org/10.1016/j.actamat.2012.11.004.
[39] S. Shu, B.D. Wirth, P.B. Wells, D.D. Morgan, G.R. Odette, Multi-technique characterization of the precipitates in thermally aged and neutron irradiated Fe-Cu and Fe-Cu-Mn model alloys: Atom probe tomography reconstruction implications, Acta Mater. 146 (2018) 237–252. https://doi.org/https://doi.org/10.1016/j.actamat.2017.12.006.
[40] M.K. Miller, K.F. Russell, Embrittlement of RPV steels: An atom probe tomography perspective, J. Nucl. Mater. 371 (2007) 145–160. https://doi.org/https://doi.org/10.1016/j.jnucmat.2007.05.003.
[41] L. Couturier, F. De Geuser, A. Deschamps, Direct comparison of Fe-Cr unmixing characterization by atom probe tomography and small angle scattering, Mater. Charact. 121 (2016) 61–67. https://doi.org/https://doi.org/10.1016/j.matchar.2016.09.028.
[42] A.J. Mauro, J.K. Sigurdsson, J. Shrake, P.J. Atzberger, S.A. Isaacson, A First-Passage Kinetic Monte Carlo method for reaction–drift–diffusion processes, J. Comput. Phys. 259 (2014) 536–567. https://doi.org/https://doi.org/10.1016/j.jcp.2013.12.023.
[43] A. Devaraj, D.E. Perea, J. Liu, L.M. Gordon, T.J. Prosa, P. Parikh, D.R. Diercks, S. Meher, R.P. Kolli, Y.S. Meng, S. Thevuthasan, Three-dimensional nanoscale characterisation of materials by atom probe tomography, Int. Mater. Rev. 63 (2018) 68–101. https://doi.org/10.1080/09506608.2016.1270728.
[44] A. Devaraj, T.C. Kaspar, S. Ramanan, S. Walvekar, M.E. Bowden, V. Shutthanandan, R.J. Kurtz, Nanoscale phase separation in epitaxial Cr-Mo and Cr-V alloy thin films studied using atom probe tomography: Comparison of experiments and simulation, J. Appl. Phys. 116 (2014) 193512. https://doi.org/10.1063/1.4901465.
[45] J. Zhou, J. Odqvist, M. Thuvander, P. Hedström, Quantitative Evaluation of Spinodal Decomposition in Fe-Cr by Atom Probe Tomography and Radial Distribution Function Analysis, Microsc. Microanal. 19 (2013) 665–675. https://doi.org/DOI: 10.1017/S1431927613000470.
[46] O.K. Chopra, A.S. Rao, Degradation of LWR Core Internal Materials due to Neutron Irradiation, 2010.
[47] Z.B. Wang, N.R. Tao, W.P. Tong, J. Lu, K. Lu, Diffusion of chromium in nanocrystalline iron produced by means of surface mechanical attrition treatment, Acta Mater. 51 (2003) 4319–4329. https://doi.org/https://doi.org/10.1016/S1359-6454(03)00260-X.
[48] Z. Li, Y. Chen, A.S. Rao, Y. Yang, Effects of Thermal Aging and Low Dose Neutron Irradiation on the Ferrite Phase in a 308L Weld, in: J.H. Jackson, D. Paraventi, M. Wright (Eds.), Proc. 18th Int. Conf. Environ. Degrad. Mater. Nucl. Power Syst. – Water React., Springer International Publishing, Cham, 2019: pp. 1905–1918.
[49] T. Oppelstrup, V. V. Bulatov, A. Donev, M.H. Kalos, G.H. Gilmer, B. Sadigh, First-passage kinetic Monte Carlo method, Phys. Rev. E - Stat. Nonlinear, Soft Matter Phys. 80 (2009) 1–14. https://doi.org/10.1103/PhysRevE.80.066701.
[50] O.C. Hellman, J.A. Vandenbroucke, J. Rüsing, D. Isheim, D.N. Seidman, Analysis of Three-dimensional Atom-probe Data by the Proximity Histogram, Microsc. Microanal. 6

(2000) 437–444. https://doi.org/DOI: 10.1007/S100050010051.
[51] J. Wang, D.K. Schreiber, N. Bailey, P. Hosemann, M.B. Toloczko, The Application of the OPTICS Algorithm to Cluster Analysis in Atom Probe Tomography Data, Microsc. Microanal. 25 (2019) 338–348. https://doi.org/DOI: 10.1017/S1431927618015386.
[52] D. Schwen, R.S. Averback, Intragranular Xe bubble population evolution in UO2: A first passage Monte Carlo simulation approach, J. Nucl. Mater. 402 (2010) 116–123. https://doi.org/10.1016/j.jnucmat.2010.05.006.
[53] G. Nandipati, Y. Shim, J.G. Amar, First-passage time approach to kinetic Monte Carlo simulations of metal (100) growth, Phys. Rev. B - Condens. Matter Mater. Phys. 81 (2010) 1–12. https://doi.org/10.1103/PhysRevB.81.235415.
[54] A. Donev, V. V. Bulatov, T. Oppelstrup, G.H. Gilmer, B. Sadigh, M.H. Kalos, A First-Passage Kinetic Monte Carlo algorithm for complex diffusion-reaction systems, J. Comput. Phys. 229 (2010) 3214–3236. https://doi.org/10.1016/j.jcp.2009.12.038.
[55] S. Hu, D.E. Burkes, C.A. Lavender, D.J. Senor, W. Setyawan, Formation mechanism of gas bubble superlattice in UMo metal fuels : Phase- fi eld modeling investigation, J. Nucl. Mater. 479 (2016) 202–215. https://doi.org/10.1016/j.jnucmat.2016.07.012.
[56] K. Hirano, M. Cohen, B.L. Averbach, Diffusion of nickel into iron, Acta Metall. 9 (1961) 440–445. https://doi.org/https://doi.org/10.1016/0001-6160(61)90138-9.
[57] F.J. BRADSHAW, G. HOYLE, K. SPEIGHT, Diffusion of Silicon in Ferrite, Nature. 171 (1953) 488. https://doi.org/10.1038/171488a0.
[58] F.S. Buffington, K. Hirano, M. Cohen, Self diffusion in iron, Acta Metall. 9 (1961) 434–439. https://doi.org/https://doi.org/10.1016/0001-6160(61)90137-7.
[59] H. Nitta, T. Yamamoto, R. Kanno, K. Takasawa, T. Iida, Y. Yamazaki, S. Ogu, Y. Iijima, Diffusion of molybdenum in α-iron, Acta Mater. 50 (2002) 4117–4125. https://doi.org/https://doi.org/10.1016/S1359-6454(02)00229-X.
[60] Y. Liu, L. Zhang, Y. Du, D. Yu, D. Liang, Atomic mobilities, uphill diffusion and proeutectic ferrite growth in Fe–Mn–C alloys, Calphad. 33 (2009) 614–623. https://doi.org/https://doi.org/10.1016/j.calphad.2009.07.002.
[61] J. Marian, B.D. Wirth, G.R. Odette, J.M. Perlado, Cu diffusion in α-Fe: determination of solute diffusivities using atomic-scale simulations, Comput. Mater. Sci. 31 (2004) 347–367. https://doi.org/https://doi.org/10.1016/j.commatsci.2004.03.023.
[62] C. Pareige, J. Emo, S. Saillet, C. Domain, P. Pareige, Kinetics of G-phase precipitation and spinodal decomposition in very long aged ferrite of a Mo-free duplex stainless steel, J. Nucl. Mater. 465 (2015) 383–389. https://doi.org/https://doi.org/10.1016/j.jnucmat.2015.06.017.
[63] J. Fukakura, M. Asano, M. Kikuchi, M. Ishikawa, Effect of thermal aging on fracture toughness of RPV steel, Nucl. Eng. Des. 144 (1993) 423–429. https://doi.org/https://doi.org/10.1016/0029-5493(93)90037-A.
[64] J. Zhou, J. Odqvist, M. Thuvander, S. Hertzman, P. Hedström, Concurrent phase separation and clustering in the ferrite phase during low temperature stress aging of duplex stainless steel weldments, Acta Mater. 60 (2012) 5818–5827. https://doi.org/https://doi.org/10.1016/j.actamat.2012.07.022.
[65] P. Franke, D. Neuschutz, Binary Systems. Part 2: Elements and Binary Systems B-C to Cr-Zr: Cu-Fe, in: Landolt-Bornstein - Gr. IV Phys. Chem., Vol 19B2, Springer Books, 2006.
[66] X.I.N. XU, J. ODQVIST, M.H. COLLIANDER, M. THUVANDER, A. STEUWER, J.E. WESTRAADT, S. KING, P. HEDSTRÖM, Structural Characterization of Phase Separation in Fe-Cr: A Current Comparison of Experimental Methods, Metall. Mater. Trans. A. 47

(2016) 5942–5952. https://doi.org/10.1007/s11661-016-3800-4.
[67] I. Shuro, H.H. Kuo, T. Sasaki, K. Hono, Y. Todaka, M. Umemoto, G-phase precipitation in austenitic stainless steel deformed by high pressure torsion, Mater. Sci. Eng. A. 552 (2012) 194–198. https://doi.org/https://doi.org/10.1016/j.msea.2012.05.030.
[68] Z.B. Jiao, J.H. Luan, M.K. Miller, Y.W. Chung, C.T. Liu, Co-precipitation of nanoscale particles in steels with ultra-high strength for a new era, Mater. Today. 20 (2017) 142–154. https://doi.org/https://doi.org/10.1016/j.mattod.2016.07.002.
[69] Z.B. Jiao, J.H. Luan, M.K. Miller, C.T. Liu, Precipitation mechanism and mechanical properties of an ultra-high strength steel hardened by nanoscale NiAl and Cu particles, Acta Mater. 97 (2015) 58–67. https://doi.org/https://doi.org/10.1016/j.actamat.2015.06.063.
[70] Q. Shen, X. Xiong, T. Li, H. Chen, Y. Cheng, W. Liu, Effects of co-addition of Ni and Al on precipitation evolution and mechanical properties of Fe-Cu alloy, Mater. Sci. Eng. A. 723 (2018) 279–286. https://doi.org/https://doi.org/10.1016/j.msea.2018.03.053.
[71] D.J. Sprouster, J. Sinsheimer, E. Dooryhee, S.K. Ghose, P. Wells, T. Stan, N. Almirall, G.R. Odette, L.E. Ecker, Structural characterization of nanoscale intermetallic precipitates in highly neutron irradiated reactor pressure vessel steels, Scr. Mater. 113 (2016) 18–22. https://doi.org/https://doi.org/10.1016/j.scriptamat.2015.10.019.
[72] B. Zhang, F. Xue, S.L. Li, X.T. Wang, N.N. Liang, Y.H. Zhao, G. Sha, Non-uniform phase separation in ferrite of a duplex stainless steel, Acta Mater. 140 (2017) 388–397. https://doi.org/https://doi.org/10.1016/j.actamat.2017.08.044.